JOURNAL OF GEOPHYSICAL RESEARCH, VOL. 107, NO. B4, 2074, 10.1029/2001JB000470, 2002

Satellite interferometric observations of displacements associated with seasonal groundwater in the Los Angeles basin

Karen M. Watson, Yehuda Bock, and David T. Sandwell

Cecil H. and Ida M. Green Institute of Geophysics and Planetary Physics, Scripps Institution of Oceanography, La Jolla, California, USA

Received 13 February 2001; revised 23 October 2001; accepted 28 October 2001; published 19 April 2002.

[1] The Newport-Inglewood fault zone (NIFZ) displays interferometric synthetic aperture radar (SAR) phase features along most of its length having amplitudes of up to 60 mm. However, interpretation in terms of right-lateral, shallow slip along the fault fails to match the range of geologic estimates of slip. Recently, *Bawden et al.* [2001] proposed that these phase features, as well as a broader deformation pattern in the Los Angeles basin, are due to vertical motion related to annual variations in the elevation of the water table. We confirm this hypothesis through the analysis of a longer span of data consisting of 26 SAR images collected by the ERS-1 and ERS-2 spacecraft between June 1992 and June 2000. Moreover, we use continuous GPS measurements from 1995 to the present to establish the amplitude and phase of the vertical deformation. The Los Angeles basin becomes most inflated one quarter of the way through the year, which is consistent with water table measurements as well as with the end of the rainy season when the aquifer should be at a maximum. The spatial pattern of the amplitude of the annual signal derived from continuous GPS measurements is consistent with the shape of the interferometric fringes. GPS sites both near the NIFZ and in a 20 by 40 km zone within the basin also show significant N-S annual variations that may be related to the differential expansion across the fault. Since these horizontal signals have peak-to-trough amplitudes of 6 mm, they mask the smaller tectonic signals and need to be taken into account when interpreting GPS time series of site position. Moreover, since the groundwater signal appears to have a long-term vertical trend which varies in sign depending on location, it will be difficult to distinguish interseismic tectonic slip along the NIFZ and within the affected areas in the basin. *INDEX TERMS:* 1206 Geodesy and Gravity: Crustal movements—interplate (8155); 1294 Geodesy and Gravity: Instruments and techniques; 1829 Hydrology: Groundwater hydrology; 1894 Hydrology: Instruments and techniques; *KEYWORDS:* Interferometric synthetic aperture radar (InSAR), Global Positioning System (GPS), groundwater seasonal deformation, subsidence, Los Angeles basin

1. Introduction

[2] The Los Angeles basin has become an area of intense focus of modern geodetic investigations since the M_W 6.8 1994 Northridge earthquake [*Hudnut et al.*, 1996]. This destructive event spurred a significant expansion of continuous GPS (CGPS) coverage in southern California, unlike the 1992 M_W 7.3 Landers earthquake that occurred in a lightly populated region and caused minor damage. The goal of regional coverage provided by the Permanent GPS Geodetic Array [*Bock et al.*, 1997] was diverted in favor of densification in the basin in an effort referred to as the Dense GPS Geodetic Array [*Hensley*, 2000]. Both arrays were later merged into a single array called the Southern California Integrated GPS Network (SCIGN; see http://www.scign.org), which now consists of more than 250 sites with a concentration of sites centered in the basin, as well as a less dense but well-distributed regional component. In parallel, the technique of interferometric synthetic aperture radar (InSAR), so successful in imaging the Landers earthquake [*Massonnet et al.*, 1993], began to be applied to studies in the basin. The Los Angeles basin turns out to be quite amenable to InSAR investigations because its widespread urban sprawl results in minimal image decorrelation (although errors due to topography and atmospheric propagation are still significant).

Copyright 2002 by the American Geophysical Union.
0148-0227/02/2001JB000470$09.00

[3] Even moderate earthquakes in the Los Angeles metropolitan region can cause significant damage, e.g., the 1971 San Fernando earthquake (M_W = 6.6), the 1987 Whittier Narrows earthquake (M_W = 6.0), the 1991 Sierra Madre earthquake (M_W = 5.6), and the 1994 Northridge earthquake (M_W = 6.8). Blind thrust faults in this region pose a significant earthquake hazard [e.g., *Dolan et al.*, 1995; *Shaw and Suppe*, 1996] but are difficult to detect, which makes quantifying the hazard difficult. One of the goals of the SCIGN array is to identify active blind thrust faults and test models of compressional tectonics in the Los Angeles basin (see http://www.scign.org).

[4] An important constraint in determining earthquake hazards for Los Angeles is the geodetically determined rate of contraction across the region. The Los Angeles basin (nearly 100 km wide and heavily populated) is contracting at a minimum rate of 4–7 mm/yr (over the last 2 m.y.) in a direction perpendicular to the San Andreas Fault, along a line from Palos Verdes to the fault [*Davis et al.*, 1989]. The orientation of these rates is normal to the dominant structural grain as evidenced by fold axes and thrust fault trends.

[5] The rate of contraction is significant in that this signal is presumed to show the rate at which faults in the region are being loaded toward eventual seismic rupture, as part of the earthquake cycle. *Dolan et al.* [1995] argue that the geodetic shortening rate of ~8.5 mm/yr across the Los Angeles metropolitan region would suggest that far too few moderate earthquakes have occurred in

response to such strain accumulation, meaning that seismic energy is possibly being stored for one or more larger earthquakes (M_W 7.2–7.6). An alternative explanation is that a significant part of this apparent strain buildup is being relieved as aseismic deformation. In this case, hazard estimates should only consider moderate earthquakes, such as have been experienced in the last 10 years, since most of the strain release would be aseismic and not accumulating toward release in large events. Recent GPS results and geological models indicate that a conjugate system of strike-slip faults with variable oblique components may accommodate as much as half of the observed shortening [*Walls et al.*, 1998]. Consequently, surface and blind thrust faults may have lower slip rates and be less of a seismic risk than some recent models imply. On the other hand, *Argus et al.* [1999] maintain that the north-south shortening is accommodated mainly by vertical crustal thickening and only minor east-west lengthening.

[6] In order to measure how the total contraction rate is accommodated within the basin it is necessary to achieve a geodetic measurement accuracy of a fraction of a millimeter per year. Combining CGPS and InSAR observations provides higher accuracy and spatial resolution than either method alone [*Bock and Williams*, 1997]. In the course of this work we initially noticed that the Newport-Inglewood fault zone (NIFZ) displayed significant interferometric phase signatures along most of its length [*Watson et al.*, 1998]. This work was motivated by our desire to understand this feature and to determine whether or not it had tectonic significance. Our investigations have led to the conclusion that quantifying small crustal deformation by geodetic means is a more difficult task than originally imagined when the decision to deploy a concentration of SCIGN stations in the basin was made.

1.1. Tectonic History

[7] The NIFZ is a narrow band of deformation ~2 km wide extending ~70 km through the Los Angeles basin from Beverly Hills at the northwest limit to Newport Beach in the southeast [*Yerkes et al.*, 1965; *Hill*, 1971; *Freeman et al.*, 1992]. It consists of a series of en echelon folds and faults. Ten short (<10 km) anticlinal folds, which trend generally westward and which accommodate a series of major oil fields, form a right-stepping en echelon series with longer (<20 km) dextral strike-slip faults which strike roughly northwest and are arranged in a left-stepping en echelon manner [*Hill*, 1971, 1974]. At depth, an unconformity in the region of the NIFZ (assumed to be a "master" dextral strike-slip fault [*Yerkes et al.*, 1965]) separates continental (Peninsular Ranges) basement material in the southwest from oceanic (Catalina Schist) to the northeast [*Hill*, 1971; *Yeats*, 1973; *Platt and Stuart*, 1974; *Yeats*, 1974; *Hauksson*, 1987]. *Wilcox et al.* [1973] used plasticene to model the NIFZ using the theory of wrench tectonics [*Harding*, 1973]. This wrenching model explained both the juxtaposition of the basement facies and the en echelon fold and fault arrangement. *Hauksson* [1987], however, believed that the surface features were instead due to north-south basin compression.

[8] Slip rates in the NIFZ have been estimated by various authors and tabulated by *Petersen and Wesnousky* [1994]. They cite a mean value of 0.6 mm/yr for the Holocene vertical slip rate and note that the dextral slip rate could be larger. *Grant et al.* [1997] estimate a minimum dextral slip of 0.35–0.55 mm/yr based on cone penetrometer tests and a rate of 1.0–3.5 mm/yr based on graben geometry. It should be noted that *Walls et al.* [1998] use a rate of 0.5 mm/yr [after *Grant et al.*, 1997] in their seismic risk assessment for the region. However, *Dolan et al.* [1995], who estimate a recurrence interval of >16,690 years for a M_W = 6.3 earthquake in the northern portion of the NIFZ, use a slip rate of <0.1 mm/yr. Currently, over 10 million people live in Los Angeles (LA) and Orange Counties. Most of that area, according to *Toppozada et al.* [1989], would fall within the modified Mercalli (MM) VII isoseismal resulting from a postulated major (M = 7) earthquake on the NIFZ.

[9] The rate of seismicity in the NIFZ is high compared to other LA basin faults of Quaternary age with similar slip rates [*Hauksson*, 1987]. The largest recorded earthquake to have occurred in the region was the M_L = 6.3 Long Beach earthquake of 10 March 1933. The earthquake left 120 people dead and many more wounded. The MM intensities of VI to IX extended from Laguna Beach north to Santa Monica and east to Whittier [*Toppozada et al.*, 1989].

[10] *Hauksson* [1987] relocated 64 earthquakes of $M_L \geq 2.5$ from 1973 to 1985 and showed that there was less scattering of seismicity about the fault than previously thought. The relocated epicenters formed a roughly northwest striking trend from Santa Monica to Dominguez Hills and then along the Los Alamitos fault. Most seismicity occurred at a depth of ~7–10 km, with a lack of seismicity shallower than 5 km. Using the focal mechanisms determined for a subset of the data (39 events), he demonstrated a variation in the stress field from north to south in the NIFZ with reverse and strike-slip mechanisms in the north indicating compression and normal and strike-slip mechanisms in the south indicating tension. This trend conflicts in the north with the fault parameters tabulated by *Barrows* [1974]. Cross sections by *Shaw and Suppe* [1996] show the NIFZ to be dipping to the northeast at angles of roughly 70° in the north (Cherry Hill fault region) to roughly 80° in the south (Seal Beach fault region), with normal slip.

1.2. Hydrologic Characteristics

[11] The NIFZ is known to separate the central and west coast groundwater basins of Los Angeles [*Nikkel et al.*, 1988]. The structure of the region is conducive to oil reservoir formation (compared to other basins, the Los Angeles basin is, globally, the largest producer of hydrocarbons per unit area [*Nilsen and Sylvester*, 1999]), and the NIFZ also creates a barrier which in some cases prevents seawater from polluting the groundwater reservoirs on the northeastern side of the zone [*Barrows*, 1973; *Testa et al.*, 1988]. It is considered, though, an incomplete barrier to water flow in the region [see *Poland*, 1959].

[12] There are three main groundwater bodies in the region of this study. They are semiperched water in strata of Holocene age; freshwater in Holocene, Pleistocene, and Pliocene deposits; and connate saline water underlying the freshwater [*Piper et al.*, 1953; *Poland et al.*, 1956]. The semiperched water is of varied chemistry and extends northeastward from the ocean via the gaps between the hills and mesas of the NIFZ. The connate saline water underlies the whole Long Beach–Santa Ana area and is separated from the freshwater body by an abrupt, largely impermeable transition. The freshwater body itself occurs in a very large volume of strata; it occurs in lower Holocene through upper Pliocene deposits [*Piper et al.*, 1953; *Poland et al.*, 1956].

1.3. Surface Deformation Across the NIFZ

[13] Results obtained by *Watson et al.* [1998] showed an InSAR phase feature in the region of the NIFZ. Since the NIFZ is an active fault zone (albeit with a low rate of deformation), our initial study centered around a tectonic source for the phase feature. Modeling showed, however, at least an order of magnitude discrepancy between the required (modeled) slip rates and those found in the literature. *Bawden et al.* [2000, 2001] postulated a nontectonic source: aquifer pumping and recharge in a seasonal cycle. They showed up to 110 mm of vertical movement and up to 15 mm of horizontal movement in InSAR and GPS observations, respectively, over the period between 1997 and 1999 in the Santa Ana basin, with focused deformation along the NIFZ. This study seeks

Table 1. Image Pairs Used for Topographic Stacking[a]

Orbits		Dates		Time Span, days	$\lvert\overline{B_\perp}\rvert$, m
Master	Slave				
E1-23705[b]	E2-04032	22 Jan. 1996	23 Jan. 1996	1	159
E2-05535	E1-25208	11 May 1996	10 May 1996	1	164
E2-03531	E1-23204	23 Dec. 1995	22 Dec. 1995	1	265
E2-02529	E1-22202	14 Oct. 1995	13 Oct. 1995	1	377
E1-11838	E1-11337	20 Oct. 1993	15 Sept. 1993	35	68
E2-11547	E2-11046	5 July 1997	31 May 1997	35	86
E2-23571	E2-24072	23 Oct. 1999	27 Nov. 1999	35	165
E2-14553	E2-14052	25 Jan. 1998	27 Dec. 1997	35	174
E2-13050	E2-13551	18 Oct. 1997	22 Nov. 1997	35	251

[a] All images are ERS-1/2 frame 2925, track 170. SAR pairs are identified by orbit number and satellite (ERS-1 (E1) or ERS-2 (E2)). $\lvert\overline{B_\perp}\rvert$ is the absolute value of the mean $B_\perp$ over the image.
[b] The master orbit.

to refine the interferometric results of *Watson et al.* [1998], correlating them with CGPS observations of SCIGN stations over the period 1993–1999, longer than that of *Bawden et al.* [2001].

2. Satellite Interferometry

2.1. InSAR and GPS

[14] CGPS and InSAR are highly complementary measurement techniques [*Bock and Williams*, 1997]. CGPS offers three-dimensional vector measurements at widely spaced points with very high temporal resolution [*Bock et al.*, 2000]. Ionospheric refraction effects on GPS signal propagation are minimized by observations at two radio frequencies, and tropospheric refraction effects can be well determined through a combination of modeling and estimation. The much greater spatial resolution of interferometric synthetic aperture radar (InSAR) (~100 m) is offset by its poor temporal sampling (>35 days), single look direction, greater susceptibility to tropospheric and ionospheric delays [*Massonnet et al.*, 1993; *Zebker et al.*, 1994; *Massonnet and Feigl*, 1998; *Rosen et al.*, 2000], and lower accuracy. Inherent errors (contributions to the phase) in the InSAR results are introduced by the atmosphere, the satellite orbits, and the topography. Methods such as stacking and using phase gradients enable minimization of these errors [see, e.g., *Sandwell and Price*, 1998]. Integrated satellite interferometry uses CGPS observations as a way to externally calibrate these InSAR errors [*Williams et al.*, 1998]. This current work follows that of *Watson et al.* [1998] and investigates InSAR phase signals occurring in the Los Angeles basin region using both geodetic tools along with supplemental data and analyses.

2.2. Interferometry

[15] The region of the NIFZ and the phase feature is included in ERS-1/2 frame 2925 track 170, which covers an area of about 100 km × 100 km extending from Santa Catalina Island in the southwest to Pomona in the northeast. Up to December 2000, there are 65 orbits available for this region, beginning in June 1992. These orbits include both the nominal ERS-1 and ERS-2 phases (with a repeat interval of 35 days per satellite) and the tandem phase (with repeat intervals of 1 day and 34 days for ERS-1 to ERS-2 and ERS-2 to ERS-1, respectively). See Figure 1 for a plot of the perpendicular baselines for all 65 orbits, referenced to E1-23705.

[16] The data used in this study were pairs of ERS-1 and/or ERS-2 synthetic aperture radar (SAR) C band (5 GHz) scenes. These raw data were processed using software developed at Stanford University and the Jet Propulsion Laboratory and since modified at the Scripps Institution of Oceanography (see *Price and Sandwell* [1998], *Sandwell and Price* [1998], and *Baer et al.* [1999] for other examples of InSAR studies using this particular software for processing). The resultant signal consists of a map of complex values representing, among other things, the range to the ground and the scattering properties of that ground. Since the satellites do not exactly repeat their orbit and hence viewing geometry each pass, each successive image will sample a slightly different region of the Earth's surface. In order to compare the same region for a deformation analysis the images must be matched by aligning them all to one reference image. We used the precise orbits generated at Delft Institute for Earth-Oriented Space Research (DEOS [see *Scharroo and Visser*, 1998]) along with an algorithm that compares the amplitudes of the pixels in the two images in order to determine shift and stretch parameters to be applied to the repeat images.

[17] Once the reference and repeat images were aligned, we took the complex value of each pixel in the reference image C_{ref} and multiplied it by the complex conjugate of the corresponding pixel value in the repeat image C_{rep} to create an interferogram:

$$R + iI = C_{\text{ref}} C^*_{\text{rep}} e^{-i\phi} \tag{1}$$

$$R + iI = A_{\text{ref}} A_{\text{rep}} e^{i\left(\phi_{\text{ref}} - \phi_{\text{rep}}\right)}, \tag{2}$$

where R is the real part of the interferogram, I is the imaginary part, and A_{ref} and A_{rep} are the amplitudes of the reference and repeat images, respectively. Using the method of *Sandwell and Price* [1998], we stacked the x and y phase gradients for 18 scenes (nine pairs) from frame 2925 track 170 using the precise DEOS orbits to derive the perpendicular baseline component $B_\perp$ for each pixel, where

$$B_\perp = B \cos\left(\theta_0 - \alpha\right) \tag{3}$$

and B is the baseline or difference between the reference and repeat images which varies along the scene, θ_0 is the look angle, and α is the baseline orientation angle (θ_0 and α both vary along and across the scene). The pairs used for topographic recovery (indicated by dashed lines in Figure 1) had short time spans of 1–35 days and $B_\perp$ ranging from 68 to 377 m (Table 1). These pairs were iteratively used to improve on U.S. Geological Survey (USGS) 1:250,000 digital elevation model (DEM) data for the region (using the method of *Sandwell and Sichoix* [2000]).

[18] The need for accurate topography is integral to InSAR. More accurate topography allows the use of interferometric pairs with longer baselines, which would otherwise be too decorrelated or corrupted by topographic phase to decipher. Further, the use of more interferograms, with varied baselines, leads to a more accurate representation of the topography, which can then be used in other ways.

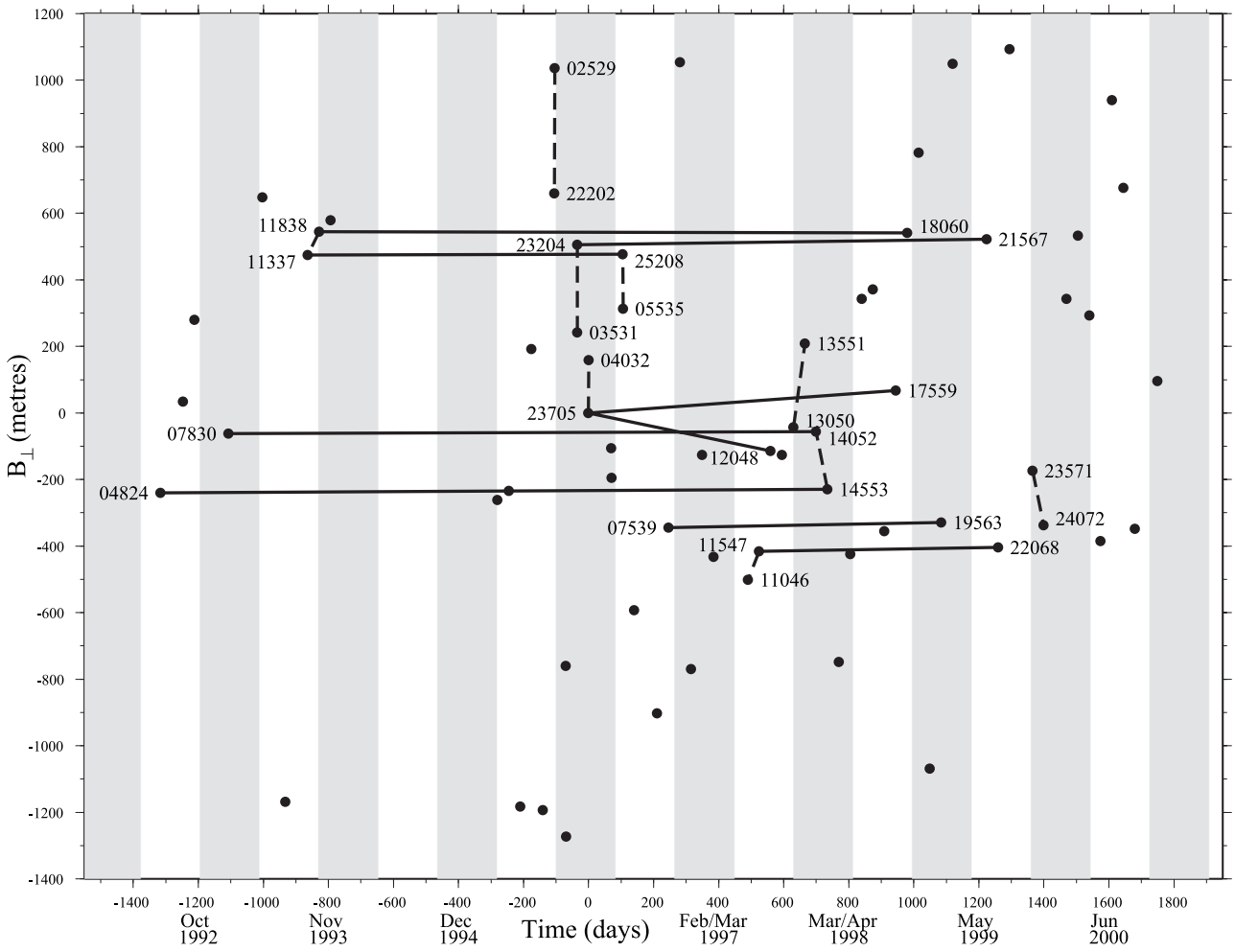

Figure 1. Perpendicular baselines for ERS-1 orbit E1-23705, frame 2925, track 170. Pairs used for stacked topographic phase are connected by dashed lines, and those used for deformation phases are connected by solid lines.

[19] In order to study deformation we differenced the SAR/DEM-derived topographic phase from nine interferometric pairs ranging in time span from 560 to 2052 days and in $B_\perp$ from 2 to 114 m (Table 2). These nine interferograms should, in theory, be free from the effects of topography. Further, the atmospheric effect in the topographic phase should have been averaged among the nine topographic pairs and therefore minimized (but the deformation phases, having been created from only one pair, will still contain the full atmospheric effect). Note that there are many more examples that can be derived, probably more than 30, considering the high number of orbits available for the region.

2.3. Results

[20] The InSAR results are shown in Figures 2 and 3. Note that the coverage of Figures 2 and 3 is only ~70 km by ~70 km (about half of the area of a regular ERS-1/2 SAR image) for clarity, since much of the rest is decorrelated or out of the focus of this

Table 2. Image Pairs Used for Deformation[a]

Orbits		Dates		Time Span, days	$\lvert\overline{B_\perp}\rvert$, m
Master	Slave				
E1-23705	E2-12048	26 Jan. 1996	9 Aug. 1997	560	114
E2-22068	E2-11547	10 July 1999	5 July 1997	735	10
E2-07539	E2-19563	28 Sept. 1996	16 Jan. 1999	839	16
E1-23705	E2-17559	26 Jan. 1996	29 Aug. 1998	945	67
E1-11337	E1-25208	15 Sept. 1993	10 May 1996	968	2
E1-11838	E2-18060	20 Oct. 1993	3 Oct. 1998	1808	2
E2-14052	E1-07830	27 Dec. 1997	13 Jan. 1993	1808	6
E1-23204	E2-21567	22 Dec. 1995	5 June 1999	1260	16
E2-14553	E1-04824	31 Jan. 1998	17 June 1992	2052	9

[a] All images are ERS-1/2 frame 2925, track 170. SAR pairs are identified by orbit number and satellite (ERS-1 (E1) or ERS-2 (E2)). $\lvert\overline{B_\perp}\rvert$ is the absolute value of the mean $B_\perp$ over the image.

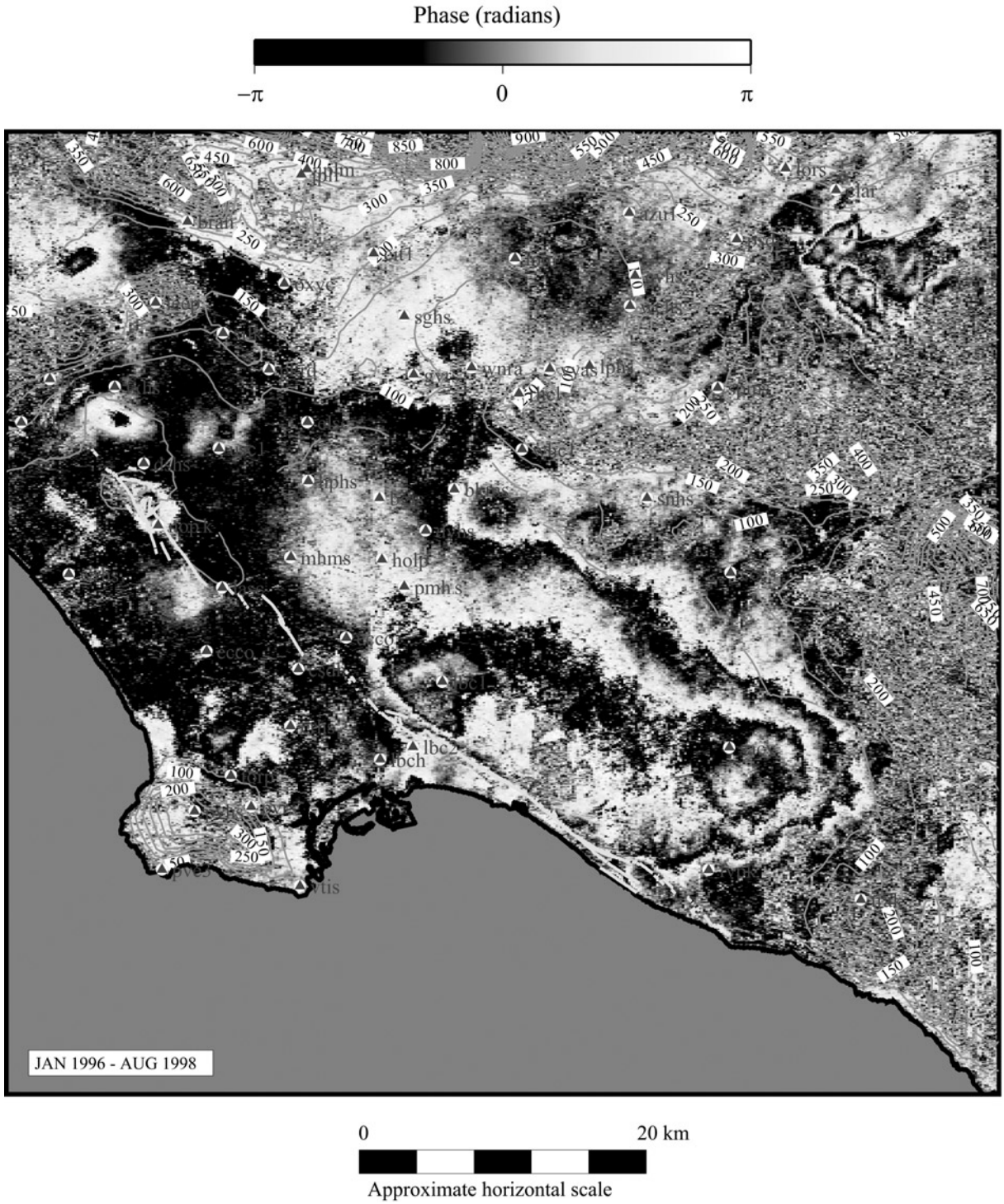

Figure 2. Excerpt of interferogram for ERS-1/2 frame 2925, track 170, orbit pair E1-23705_E2-17559. Also plotted are the coastline (black), SCIGN stations (red), 50-m topographic contours (green), and the NIFZ (yellow). See color version of this figure at back of this issue.

discussion. We see a large phase feature coincident with the NIFZ in over half of the interferograms (E1-23705_E2-17559, E2-14553_E1-04824, E2-07539_E2-19563, E1-23705_E2-12048, E1-23204_E2-21567, and E1-11838_E2-18060). The feature appears to be well defined in the region of the Long Beach to Newport Beach segment of the NIFZ and shows a striking correlation along its SE boundary with the trace of the NIFZ. Overall, the wrapped phase appears as an elliptical-shaped signal, with an amplitude of up to two fringes of phase (56 mm of deformation in the line-of-sight direction of the radar, which correlates to 61 mm of vertical deformation (uplift/subsidence depending on the epoch)). Comparing the interferograms and time periods for E2-14052_E1-07830 (19971227_19930113 = 1808 days) that does not show the feature and E2-14553_E1-04824

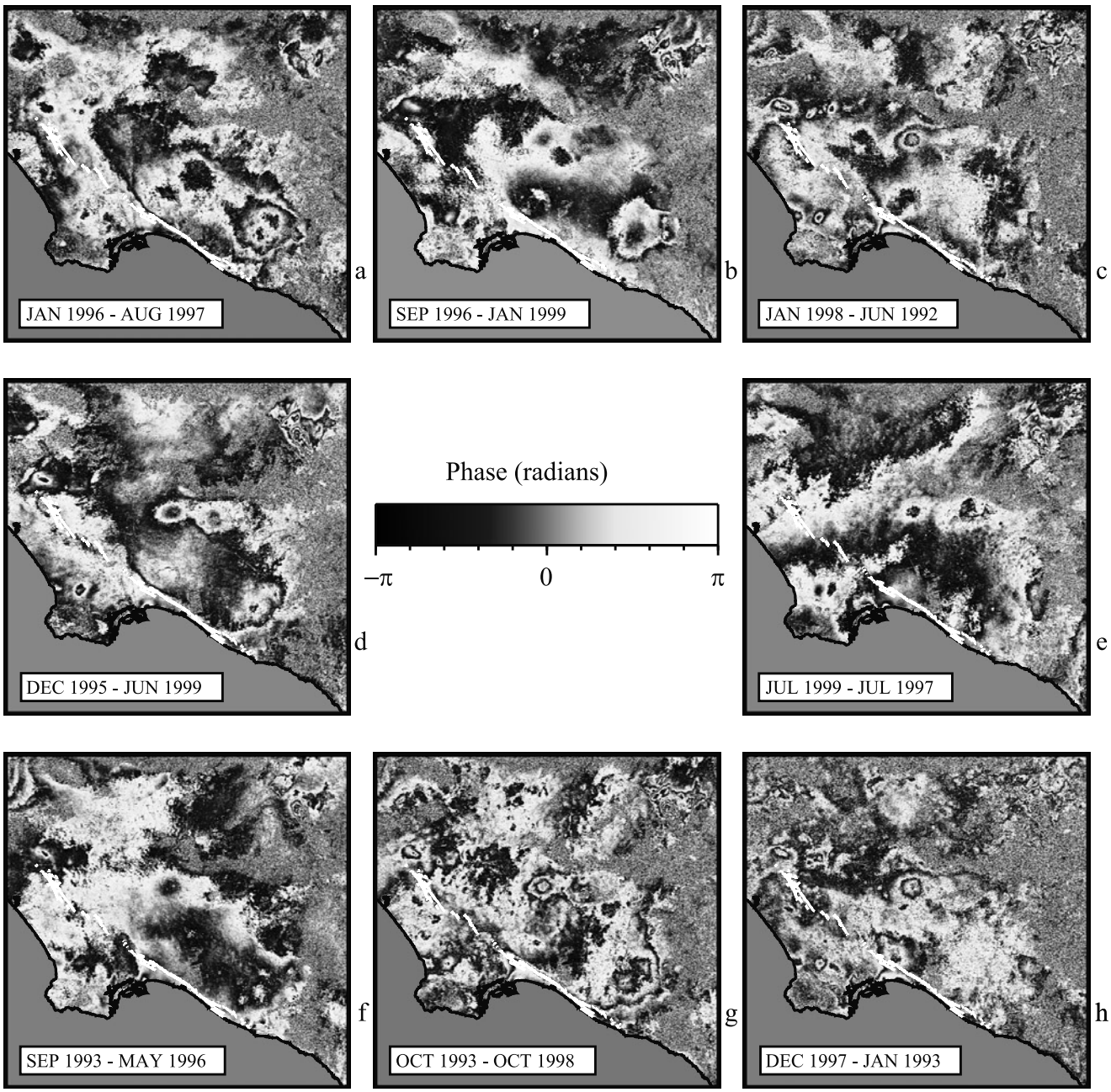

Figure 3. Excerpts of remaining interferograms: (a) E1-23705_E2-12048, (b) E2-07539_E2-19563, (c) E2-14553_E1-04824, (d) E1-23204_E2-21567, (e) E2-22068_E2-11547, (f) E1-11337_E1-25208, (g) E1-11838_E2-18060, and (h) E2-14052_E1-07830. Also plotted are the coastline (black) and the NIFZ (white).

(19980131_19920617 = 2052 days, overlapping the prior epoch) that does, we come to the conclusion that the feature must be generated in the extra 244 days, indicating a possible transient deformation source.

[21] On closer inspection of the InSAR images and GPS time series (below), we find an annual cycle to the vertical deformation having a peak one quarter of the way through the year and a trough three quarters of the way through the year. Interferograms with spring to fall time spans show the largest signal, while time intervals of exactly 1 year have small signals. The only exception to this observation is E1-11838_E2-18060 (1808 days = 4.95 years), which shows over one fringe of phase (Figure 3g). Since the fringes occur in areas where the topography is flat, a topographic error cannot be responsible. Indeed, since the flat areas are basins, it may imply a hydrological cause, as proposed by *Bawden et al.* [2001].

3. Discussion

3.1. Hydrology and GPS

[22] To further evaluate the annual signal, we analyzed meteorological data using the total monthly surface precipitation (TPCP) data obtained online from the National Virtual Data System (http://www.nvds.noaa.gov). Plots showing the precipitation per month were prepared. The data show a consistent yearly peak in the January–February region. During the period covered by the InSAR analysis (17 June 1992 to 5 June 1999), there were three consistent maxima occurring both in the regions southwest of

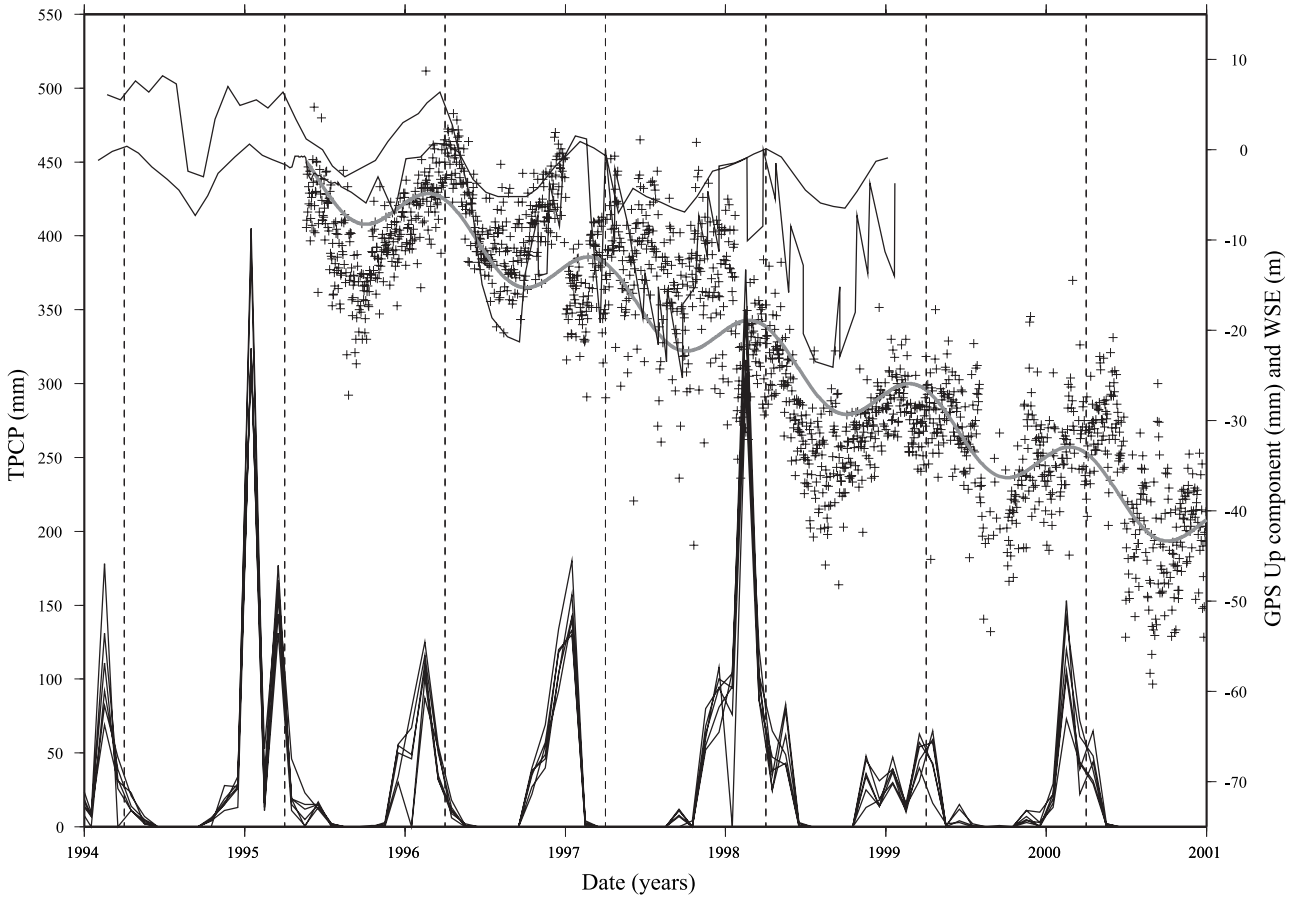

Figure 4. Plot of GPS Up component (in mm) for SCIGN site HOLP (pluses) with least squares fit sinusoidal curve for HOLP overlain (shaded curve). Plot of total monthly precipitation (TPCP) (in mm) for six meteorological stations in the region, bottom curves. Plot of groundwater surface elevation (WSE) (in m) for two stations (locations shown by star in Figures 6 and 7), top curves. Dashed vertical lines are drawn at *i*.25 years.

and northeast of the NIFZ. These maxima occurred in January 1993, January 1995, and February 1998.

[23] We also analyzed groundwater data using water surface elevation (WSE) data obtained from three sources: both offline (courtesy of G. Gilbreath, personal communication, 2000) and online from the California Department of Water Resources (http://well.water.ca.gov), and offline from the Los Angeles County Department of Public Works (courtesy of M. Utley, personal communication, 2000). Comparisons of groundwater levels for each of the InSAR epochs were created on a 20-day basis for the master and slave passes. (Data for 10 days before each pass and 10 days after each pass were averaged.) The differences were then contoured and compared to the interferograms. These contour plots of differential groundwater showed no similarity to the respective interferograms. However, when groundwater surface elevation (WSE) time series were plotted with GPS up component and precipitation TPCP time series (Figure 4), a clear correlation could be seen. It appears that in general, a maximum WSE and up sine curve amplitude occurs following a maximum precipitation rate. The offset in the precipitation and the seeming response of the WSE and GPS is about one quarter of a year ($\pi/2$ = 3 months), which is what would be expected if they are indeed responding to a maximum water flux in the region due to the precipitation. Since the interferometric phase and GPS signals occur in the same region NE of the NIFZ and do not cross the NIFZ, it implies that the NIFZ does indeed form a watertight barrier in the region. The Talbert water-bearing zone, which underlies the region and should facilitate water flow, seems ineffective.

[24] We further investigated the effect on both the vertical and horizontal GPS data. As shown in Figures 5 and 6, there is a strong annual sinusoidal signal in the GPS up component values for sites close to, and on the NE side of, the NIFZ. This signal is also apparent in the north components (Figures 7 and 8a) but at smaller amplitudes. No such signal is readily apparent in the east component (Figure 8b). Note that there are also linear trends in the up time series, which are indicative of vertical deformation, but there is no consistent direction, up or down.

[25] We modeled the time series trends using the method of least squares to estimate the amplitude (A) and phase (ϕ) of a sinusoidal curve fit to the up (U) time series:

$$U = A \sin[2\pi(t + \phi)] + mt + c \tag{4}$$

$$U = a \sin(2\pi t) + b \cos(2\pi t) + mt + c, \tag{5}$$

where t is the time (years), m is the gradient of the linear slope, and c is a constant. The estimated amplitudes and phases, like the TPCP and WSE comparisons, were then contoured.

[26] The amplitudes of least squares-derived sine curve fits to the up components for sites in the region with time series longer than 1.5 years (except SACY, which is just over 1 year long) are shown as a contour map in Figure 9. The spatial character of the contours shows a remarkable consistency with the major InSAR feature on the NW side of the NIFZ (compare to Figures 2 and 3).

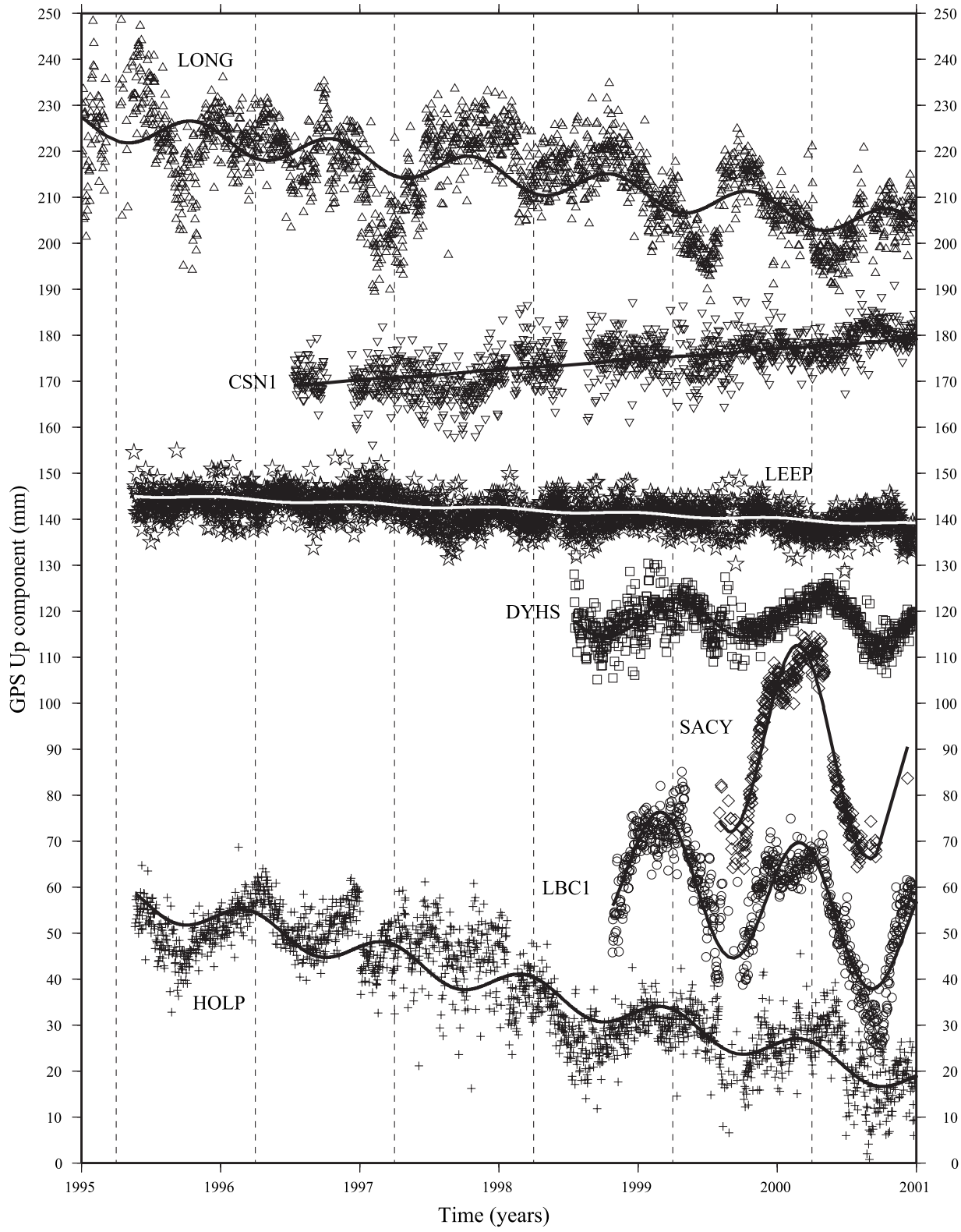

Figure 5. Plot of GPS UP component for SCIGN sites LONG (triangle), CSN1 (inverted triangle), LEEP (star), DYHS (square), SACY (diamond), LBC1 (circle), and HOLP (plus). The respective least squares fit sinusoidal curves are overlain. Dashed vertical lines drawn at *i*.25 years. Note that offsets have been applied to each time series for plot clarity.

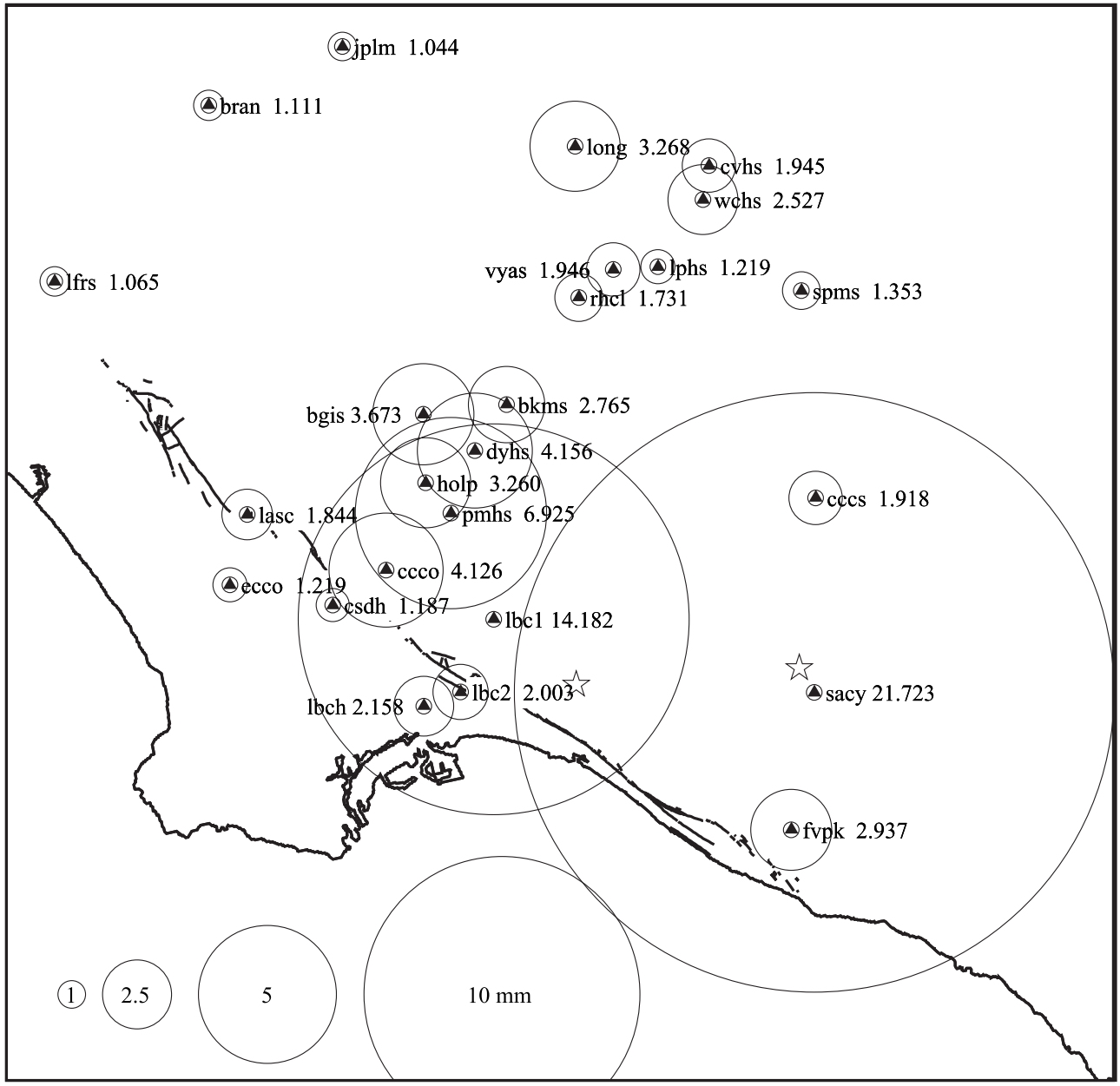

Figure 6. Plot of up component least squares fit sinusoidal curve amplitudes $\geq$1.0 mm. Note that amplitudes (in mm) are shown beside site names, and circle radii scale with amplitude. Wells with time series in Figure 4 shown by star.

Further, the amplitude of the curve for the station SACY (maximum for the region) is 14.7 mm (Table 3) which would translate to roughly one phase fringe in an interferogram covering a minimum to maximum (or vice versa) period. This is only half the maximum amplitude of the feature seen in the interferograms (about two fringes). However, the least squares method used might underestimate the amplitudes, especially if there are periodic components other than a purely annual signal (see Figures 5 and 7). A similar contour plot is overlain for the least squares-derived phases. These phase values indicate that other regions are unrelated, either because they have a different phase or they are located in a different region.

[27] Since the effect on the up component of the GPS time series in the region of the NIFZ closely follows a sinusoidal curve with a delay of $\pi/2$ (3 months), a correction could (and should) conceivably be applied to the series (and to a lesser extent to the north series). Further, the implications for seismic risk in the region of the movement beside the fault should be studied. InSAR features on a smaller spatial scale may also be seen in the Wilmington oil field area. These features are due to fluid input and withdrawal and can be successfully modeled using subsidence contour data from the California Department of Conservation [see, e.g., *Guerard*, 1999]. The NIFZ feature would seem to be similar (ground surface response to underground fluid level fluctuations) but on a much larger scale. *Galloway et al.* [1998] also used InSAR to demonstrate groundwater level change in the Antelope Valley.

3.2. Atmospheric Considerations

[28] The zenith neutral delay (ZND) gives a representation of possible atmospheric effects on SAR images [see, e.g.,

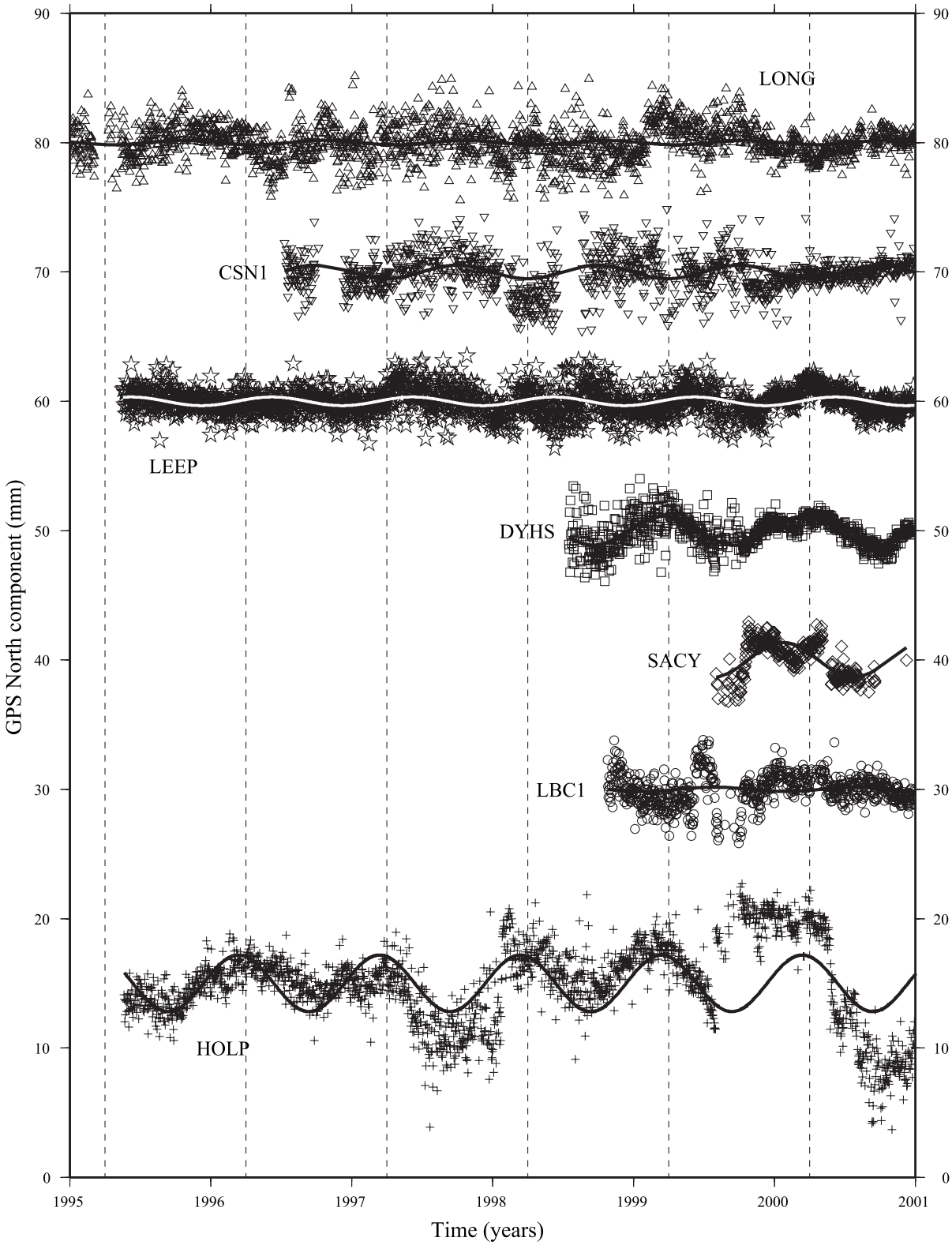

Figure 7. Plot of GPS North component for SCIGN sites LONG (triangle), CSN1 (inverted triangle), LEEP (star), DYHS (square), SACY (diamond), LBC1 (circle) and HOLP (plus). Dashed vertical lines drawn on all plots at *i*.25 years. Note that a linear trend has been removed from each of these north time series, and offsets have been applied for plot clarity.

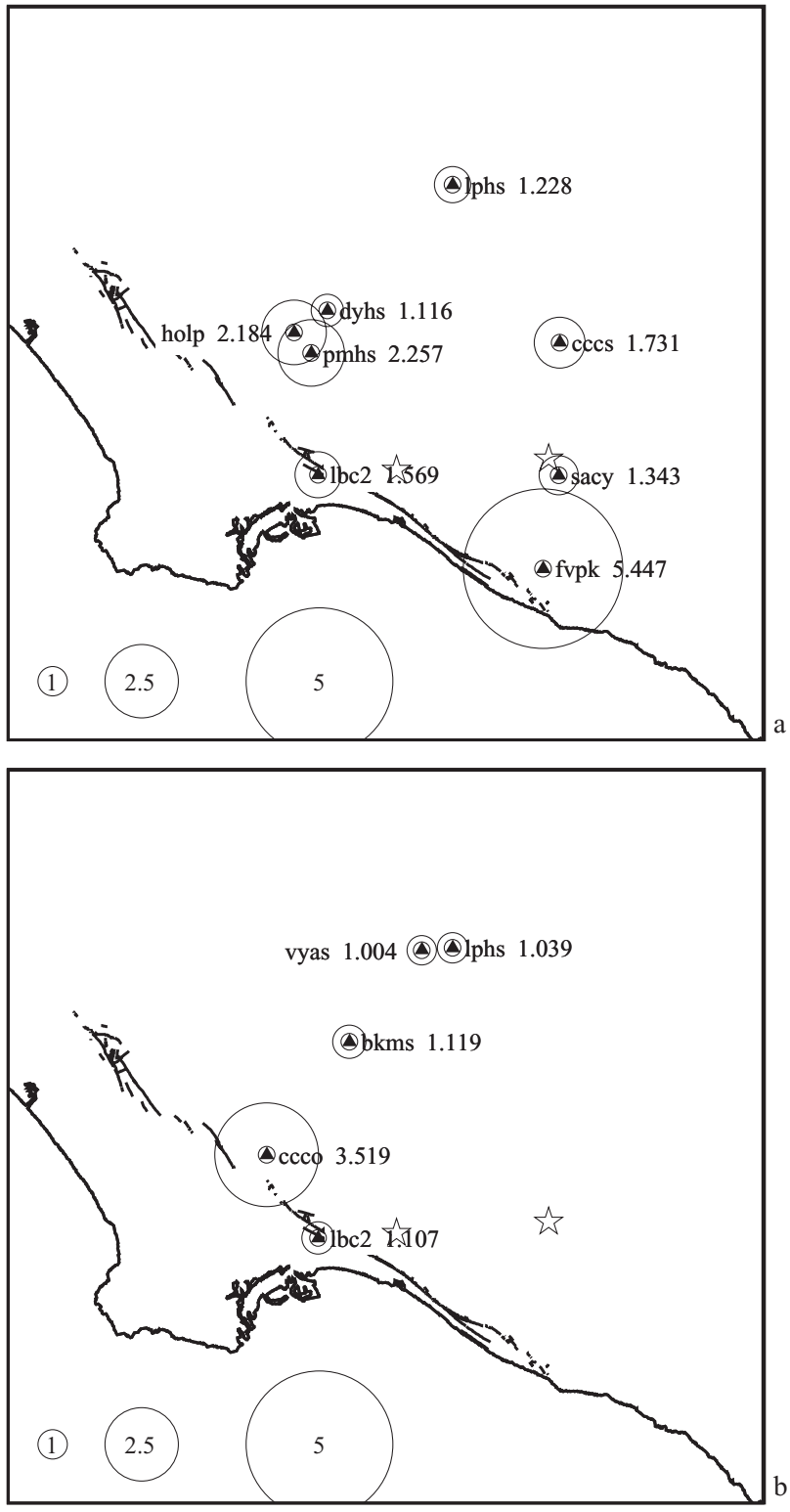

Figure 8. (a) Plot of north component least squares fit sinusoidal curve amplitudes $\geq$1.0 mm. Note that amplitudes (in mm) are shown beside site names and circle radii scale with amplitude. Wells with time series in Figure 4 are shown by star. (b) Plot of east component least squares fit sinusoidal curve amplitudes $\geq$1.0 mm. Circle radii scale with amplitude. Wells with time series in Figure 4 are shown by star.

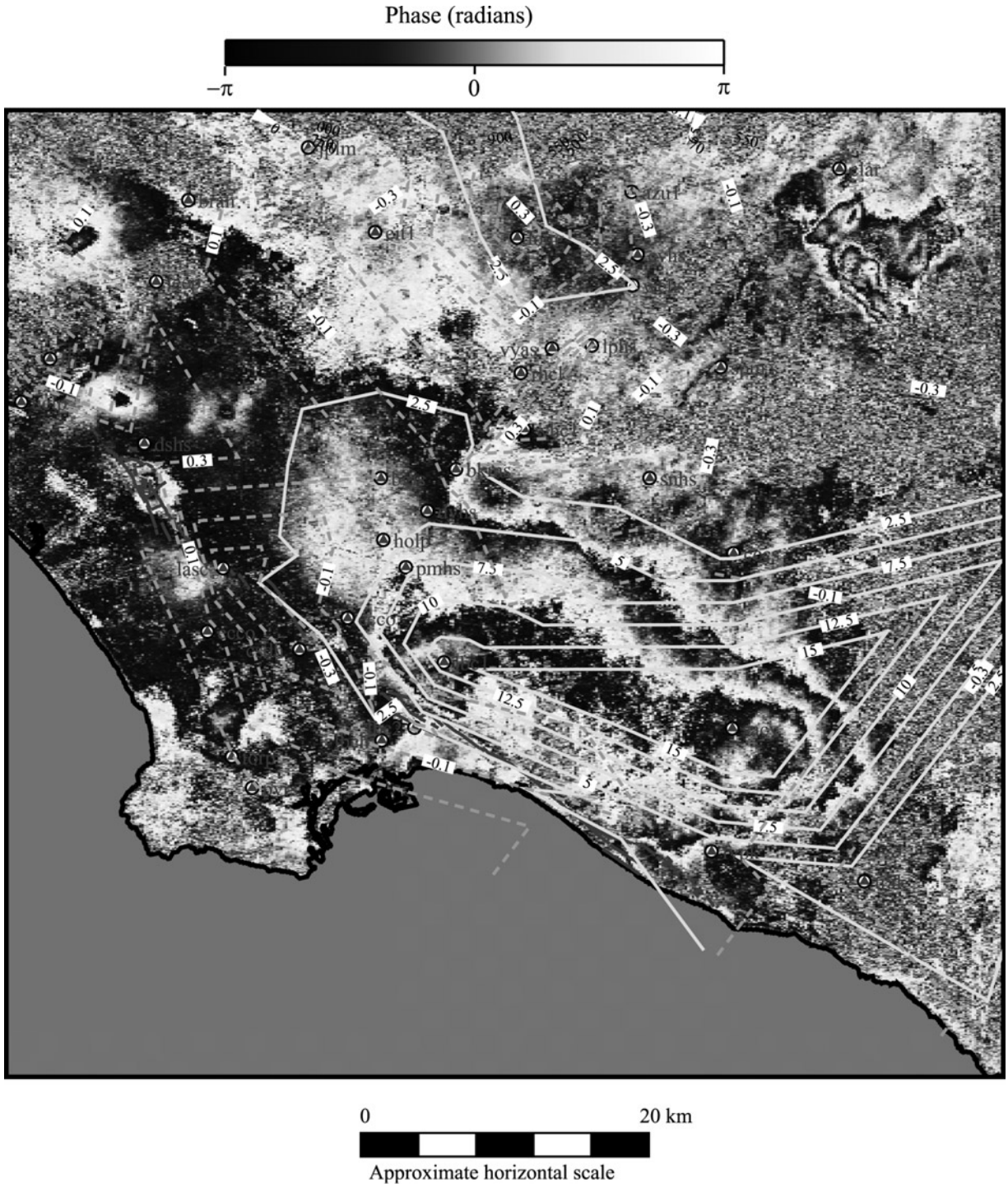

Figure 9. Contour plot of up component least squares fit sinusoidal curve amplitudes (yellow solid lines) in mm and phase (green dashed lines) in years for the SCIGN sites labeled. See color version of this figure at back of this issue.

Williams et al., 1998]. Hence ZND data derived from GPS solutions were investigated. An average of the hourly data for the two GPS epochs occurring about the SAR satellite flyover time was determined for those SAR passes which had corresponding GPS data. The data from the master SAR pass was subtracted from the data of the slave SAR pass, and a comparison map of differenced ZND was plotted. The map was then compared to the relevant interferogram. We also looked for any large differences between the ZND values for sites on different sides of the NIFZ. Unfortunately, there were little or no ZND results available for the region for the earliest epochs (pre-1994).

[29] The maximum ZND difference across the NIFZ was ~42 mm between sites PVEP and TRAK for the orbit pair E1-23705_E2-12048 (6 December 1996 to 9 August 1997). This maps into ~85 mm of two-way delay in the line of sight of the

Table 3. Least Squares Fit Sinusoidal Curve Amplitude and Phase Values for GPS Up Component Time Series

Site	Latitude	Longitude	Elevation, m	A, mm	σ_A, mm	ϕ, years	σ_ϕ, years	m, mm/yr	σ_m, mm/yr	Length, years
azu1	−117.896484	34.126018	144.76	0.235	0.152	−0.3108	0.3097	0.945	0.091	4.481
bgis	−118.159694	33.967117	2.83	3.673	0.239	0.0918	0.0095	1.546	0.328	1.762
bkms	−118.094695	33.962257	11.00	2.765	0.253	−0.1518	0.0153	5.568	0.254	2.436
bran	−118.277047	34.184893	246.24	1.111	0.188	0.2241	0.0276	−1.966	0.078	6.112
ccco	−118.211195	33.876258	−16.93	4.126	0.245	0.0001	0.0086	1.083	0.307	1.942
cccs	−117.864940	33.862741	31.83	1.918	0.351	−0.1309	0.0307	9.622	0.468	1.942
chil	−118.025997	34.333422	1567.51	0.405	0.287	0.4463	0.1153	4.179	0.113	6.359
cit1	−118.127283	34.136708	215.33	0.316	0.130	−0.4504	0.0660	0.765	0.056	6.348
cjms	−117.479381	34.313798	933.36	0.933	0.821	−0.0915	0.1340	21.183	0.984	2.044
clar	−117.708807	34.109927	373.63	0.831	0.160	0.1426	0.0301	1.370	0.068	5.737
cmp9	−118.411422	34.353179	1138.02	3.001	0.830	0.3440	0.0449	−15.476	0.368	5.559
crfp	−117.099680	34.039051	688.81	1.975	0.186	−0.3213	0.0147	0.400	0.069	6.584
csdh	−118.256714	33.861476	−9.17	1.187	0.192	−0.4560	0.0245	3.703	0.180	2.507
csn1	−118.523809	34.253549	261.43	0.084	0.204	0.2343	0.1301	2.626	0.111	4.489
cvhs	−117.901714	34.082010	119.10	1.945	0.206	−0.3407	0.0159	1.440	0.198	2.471
dshs	−118.348539	34.023930	−2.11	0.694	0.169	0.4374	0.0403	−2.353	0.259	1.644
dyhs	−118.125979	33.937987	1.47	4.156	0.215	−0.0139	0.0080	−0.061	0.204	2.496
ecco	−118.329023	33.886751	−19.35	1.219	0.175	0.2059	0.0240	0.110	0.257	1.745
ewpp	−117.525582	34.104197	330.48	2.479	0.235	−0.4505	0.0139	−1.599	0.314	1.827
fvpk	−117.935711	33.662325	−11.53	2.937	0.195	−0.0411	0.0117	1.428	0.218	2.285
holp	−118.168168	33.924538	−6.69	3.260	0.432	0.0493	0.0202	−7.019	0.184	5.652
jplm	−118.173224	34.204819	423.98	1.044	0.349	0.3166	0.0536	4.467	0.109	8.541
lasc	−118.306502	33.927941	24.69	1.844	0.179	−0.4240	0.0121	0.723	0.170	2.244
lbc1	−118.137180	33.832068	−21.94	14.182	0.785	0.0808	0.0072	−6.651	0.757	2.219
lbc2	−118.173239	33.791608	−28.47	2.003	0.295	−0.3221	0.0224	6.442	0.311	2.219
lbch	−118.203340	33.787769	−27.57	2.158	0.458	−0.1374	0.0340	−6.348	0.188	6.452
leep	−118.321752	34.134600	485.05	0.333	0.113	0.2611	0.0552	−1.135	0.049	5.660
lfrs	−118.412822	34.095069	146.90	1.065	0.212	−0.4924	0.0288	2.900	0.291	1.729
long	−118.003407	34.111899	74.27	3.268	0.328	0.4428	0.0157	−3.812	0.133	6.156
lphs	−117.956717	34.026768	68.51	1.219	0.188	0.3021	0.0225	−0.226	0.162	2.436
math	−117.436813	33.856685	396.88	2.700	0.437	−0.3618	0.0256	4.902	0.143	7.679
msob	−117.210123	34.230844	1733.15	4.795	0.349	−0.3717	0.0108	3.650	0.409	2.167
oat2	−118.601377	34.329891	1112.59	1.695	0.403	−0.4937	0.0373	6.808	0.167	5.940
pmhs	−118.153683	33.902633	−11.13	6.925	0.287	0.0477	0.0063	0.244	0.275	2.436
ppbf	−117.182086	33.835725	428.10	2.230	0.258	−0.4622	0.0142	1.729	0.279	2.044
pvrs	−118.320585	33.773861	59.83	0.724	0.211	0.3147	0.0511	2.151	0.292	1.937
rhcl	−118.026167	34.019050	176.88	1.731	0.208	−0.4917	0.0175	1.669	0.274	1.827
rths	−117.353332	34.089149	328.69	1.782	0.344	−0.4078	0.0291	4.262	0.337	2.767
sacy	−117.895575	33.743244	−11.24	21.723	1.364	0.0962	0.0138	−5.959	4.769	1.351
scms	−117.634560	33.444139	23.26	3.955	0.408	−0.4181	0.0142	−5.934	0.399	2.337
snhs	−117.928625	33.927336	66.43	0.289	0.208	−0.4960	0.1024	3.210	0.288	1.742
spms	−117.848772	33.992653	207.04	1.353	0.191	−0.3269	0.0210	2.492	0.184	2.340
torp	−118.330601	33.797797	−5.21	0.675	0.198	0.3051	0.0517	0.715	0.175	2.852
trak	−117.803432	33.617934	115.55	0.401	0.301	−0.3647	0.1159	−4.139	0.108	6.606
uclp	−118.441907	34.069120	111.55	0.701	0.116	0.4664	0.0266	−0.919	0.049	5.855
usc1	−118.285112	34.023950	21.93	1.918	0.218	−0.2506	0.0179	−3.032	0.091	5.855
vyas	−117.992048	34.030915	56.46	1.946	0.221	−0.4899	0.0171	−1.817	0.211	2.436
wchs	−117.911108	34.061897	100.11	2.527	0.235	−0.4216	0.0130	1.329	0.282	1.970
whc1	−118.031166	33.979884	94.28	0.556	0.293	0.4818	0.0839	−5.075	0.124	5.775
wlsn	−118.055910	34.226120	1705.25	3.420	0.233	−0.0143	0.0106	0.922	0.153	5.677

radar, or about three phase fringes. The maximum difference in pair E1-23705_E2-17559 (26 January 1996 to 29 August 1998) was ∼15 mm for PVEP/TRAK, or about one fringe. Unfortunately, both PVEP and TRAK appear in decorrelated regions of the interferograms, so no direct comparison could be made between the InSAR and ZND results. However, stations USC1 and HOLP (and LBCH) do appear in correlated regions of the interferograms. These two sites have approximate ZND differences of about one half of a fringe and less than one sixth for pair E1-23705_E2-17559, about one tenth and more than one half for E2-07539_E2-19563, and about one sixth and one seventieth for E1-23705_E2-12048, respectively. These ZND-derived phase differences agree with the interferograms for station USC1 but not for station HOLP. Overall, the ZND contour plots did not match the interferograms, but the data set was rather sparse. As a result, we cannot rule out the possibility that ZND effects are responsible, at least in part, for the phase features seen in the interferograms. *Watson* [2001] discusses these and other results in more depth.

4. Conclusions and Future Work

[30] Our results confirm the hypothesis of *Bawden et al.* [2001] that the 60-mm amplitude periodic interferometric phase signature along the NIFZ and in a zone of about 20 km by 40 km to the northeast has an annual cycle. Continuous GPS measurements clearly display the annual cycle, while the spatial extent of the groundwater surface deformation is most apparent in interferograms having spring to fall time spans. Contours of the amplitude and phase of the annual signal derived from GPS are in remarkable agreement with the vertical motions derived from InSAR in this zone.

[31] The broad signature associated with such a shallow source implies that the water table achieves hydrostatic equili-

brium on timescales much shorter than 1 year. This signal is of hydrologic importance and could be used to assess groundwater recharge and usage. The sharp interferometric phase gradient across the NIFZ is consistent, therefore, with a model where the fault acts as a barrier to groundwater. Annual variation in groundwater on the northeast side of the NIFZ causes volumetric expansion of the sediments that appear to induce both vertical and horizontal differential motions across the fault. Oddly, the horizontal motions are not just confined to the NIFZ but correlate to areas where annual vertical motions are greatest.

[32] The presence of large annual signals of hydrologic origin in the southeastern part of the Los Angeles basin will need to be taken into account when interpreting the geodetic data for tectonic motion. For GPS, amplitudes of annual vertical displacements are significant for at least 11 SCIGN sites and range from 3 to 22 mm in the affected zone with an uncertainty of only a fraction of a millimeter, as well as for other sites distributed over a larger part of the basin in the range of 1–3 mm (Figure 6). Furthermore, amplitudes of annual horizontal motions are ~1–2 mm, primarily in the north direction away from the NIFZ (Figure 8a) but only in the affected zone. This is considerable, however, since the entire horizontal signal (i.e., the contraction rate) in the Los Angeles basin is only ~7–8 mm/yr, and we are seeking to detect horizontal displacement rates with submillimeter precision. Most disturbingly, some GPS sites within this zone show a long-term vertical trend (both up and down) that may be related to secular trends in groundwater levels and may mask interseismic tectonic signals such as would be related to vertical crustal thickening hypothesized by *Argus et al.* [1999].

[33] To address these issues, it is clear that we will need to take better advantage of the strengths of both GPS and InSAR. For example, the dense GPS coverage in the basin can be use to calibrate the InSAR measurements for tropospheric, ionospheric, and orbital errors, but this approach has not yet been fully exploited. We need to analyze more interferometric images to further improve our determination of the topography, to reduce tropospheric effects, and to better identify zones with significant nontectonic signatures. The continuous GPS time series are still short at most sites, and the SCIGN network is only now reaching its full complement in the basin. Finally, we need to make more comparisons with hydrologic data.

[34] **Acknowledgments.** This work benefited from discussions with Duncan Agnew, Gerald Bawden, Wayne Thatcher, Peng Fang, and Matthijs van Domselaar. Synthetic aperture radar data were provided by the European Space Agency through their North American distributors, SpotImage and Eurimage. We acknowledge the Southern California Integrated GPS Network and its sponsors, the W. M. Keck Foundation, NASA, NSF, USGS, and SCEC, for providing data used in this study. We thank our colleagues at the Scripps Orbit and Permanent Array Center (SOPAC) for access to the CGPS position time series. This work was supported by the National Science Foundation and NASA (EAR9619201). SAR data were purchased by NASA and NSF (EAR9619201) and were later contributed to the WInSAR consortium. This research was also supported by the Southern California Earthquake Center. SCEC is funded by NSF Cooperative Agreement EAR-8920136 and USGS Cooperative Agreements 14-08-0001-A0899 and 1434-HQ-97AG01718. SCEC contribution 623.

References

Argus, D. F., M. B. Heflin, A. Donnellan, F. H. Webb, D. Dong, K. J. Hurst, D. C. Jefferson, G. A. Lyzenga, M. M. Watkins, and J. F. Zumberge, Shortening and thickening of metropolitan Los Angeles measured and inferred by using geodesy, *Geology*, *27*, 703–706, 1999.

Baer, G., D. Sandwell, S. Williams, Y. Bock, and G. Shamir, Coseismic deformation associated with the November 1995, M_W = 7.1 Nuweiba earthquake, Gulf of Elat (Aqaba), detected by synthetic aperture radar interferometry, *J. Geophys. Res.*, *104*, 25,221–25,232, 1999.

Barrows, A. G., Earthquakes along the Newport-Inglewood structural zone, *Calif. Geol.*, *26*, 60–68, 1973.

Barrows, A. G., A review of the geology and earthquake history of the Newport-Inglewood structural zone, southern California, *Spec. Rep. 114*, 115 pp., Calif. Div. of Mines and Geol., Sacramento, 1974.

Bawden, G. W., W. Thatcher, R. S. Stein, C. Wicks, K. Hudnut, and G. Peltzer, Ground water pumping masks tectonic deformation near Los Angeles, California, *Eos Trans. AGU*, *81*(48), Fall Meet. Suppl., Abstract H21G-05, 2000.

Bawden, G. W., W. Thatcher, R. S. Stein, C. Wicks, K. Hudnut, and G. Peltzer, Tectonic contraction across Los Angeles after removal of groundwater pumping effects, *Nature*, *412*, 812–815, 2001.

Bock, Y., and S. Williams, Integrated satellite interferometry in southern California, *Eos Trans. AGU*, *78*, 293, 299–300, 1997.

Bock, Y., et al., Southern California permanent GPS geodetic array: Continuous measurements of regional crustal deformation between the 1992 Landers and 1994 Northridge earthquakes, *J. Geophys. Res.*, *102*, 18,013–18,033, 1997.

Bock, Y., R. M. Nikolaidis, P. J. de Jonge, and M. Bevis, Instantaneous geodetic positioning at medium distances with the Global Positioning System, *J. Geophys. Res.*, *105*, 28,223–28,253, 2000.

Davis, T. L., J. Namson, and R. F. Yerkes, A cross section of the Los Angeles area: Seismically active fold and thrust belt, the 1987 Whittier Narrows earthquake, and earthquake hazard, *J. Geophys. Res.*, *94*, 9644–9664, 1989.

Dolan, J. F., K. Sieh, T. K. Rockwell, R. S. Yeats, J. Shaw, J. Suppe, G. J. Huftile, and E. M. Gath, Prospects for larger or more frequent earthquakes in the Los Angeles metropolitan region, *Science*, *267*, 199–205, 1995.

Freeman, S. T., E. G. Heath, P. D. Guptill, and J. T. Waggoner, Seismic hazard assessment, Newport-Inglewood fault zone, in *Engineering Geology Practice in Southern California*, edited by B. W. Pipkin and R. J. Proctor, *Spec. Publ. 4*, pp. 211–231, Assoc. of Eng. Geol., South. Calif. Sect., Belmont, Calif., 1992.

Galloway, D. L., K. W. Hudnut, S. E. Ingebritsen, S. P. Phillips, G. Peltzer, F. Rogez, and P. A. Rosen, Detection of aquifer system compaction and land subsidence using interferometric synthetic aperture radar, Antelope Valley, Mojave Desert, California, *Water Resour. Res.*, *34*, 2573–2585, 1998.

Grant, L. B., J. T. Waggoner, T. K. Rockwell, and C. von Stein, Paleoseismicity of the North Branch of the Newport-Inglewood fault zone in Huntington Beach, California, from cone penetrometer test data, *Bull. Seismol. Soc. Am.*, *87*, 277–293, 1997.

Guerard, W. F., 1998 annual report of the State Oil and Gas Supervisor, Rep. PR 06, 269 pp., Calif. Dep. of Conserv., Div. of Oil, Gas, and Geotherm. Resour., Sacramento, 1999.

Harding, T. P., Newport-Inglewood trend, California—An example of wrenching style of deformation, *Am. Assoc. Pet. Geol. Bull.*, *57*, 97–116, 1973.

Hauksson, E., Seismotectonics of the Newport-Inglewood fault zone in the Los Angeles basin, southern California, *Bull. Seismol. Soc. Am.*, *77*, 539–561, 1987.

Hensley, E., A SCIGN before its Time, A history of the southern California integrated GPS network, *South. Calif. Earthquake Cent. Q. Newsl.*, *5*, 4–11, 25–31, 2000.

Hill, M. H., Newport-Inglewood zone and Mesozoic subduction, California, *Geol. Soc. Am. Bull.*, *82*, 2957–2962, 1971.

Hill, M. H., The Newport-Inglewood zone of dDeformation, in *Guidebook to Selected Features of Palos Verdes Peninsula and Long Beach, California*, edited by M. S. Woyski, pp. 32–35, South Coast Geol. Surv., Irvine, Calif., 1974.

Hudnut, K. W., et al., Coseismic displacements of the 1994 Northridge, California, earthquake, *Bull. Seismol. Soc. Am.*, *86*, 19–36, 1996.

Massonnet, D., and K. Feigl, Radar interferometry and its application to changes in the Earth's surface, *Rev. Geophys.*, *36*, 441–500, 1998.

Massonnet, D., M. Rossi, C. Carmona, F. Adragna, G. Peltzer, K. Feigl, and T. Rabaute, The displacement field of the Landers earthquake mapped by radar interferometry, *Nature*, *364*, 138–142, 1993.

Nikkel, M., T. Mueller, K. Thompson, and P. Rechard, Assessment of the adequacy of the ground-water monitoring system for artificial recharge of aquifers in the Los Angeles area, California, report, pp. 45–69, Assoc. of Ground Water Sci. and Eng., Westerville, Ohio, 1988.

Nilsen, T. H., and A. G. Sylvester, Strike-slip basins, part 2, *Leading Edge*, *18*, 1258–1267, 1999.

Petersen, M. D., and S. G. Wesnousky, Fault slip rates and earthquake histories for active faults in southern California, *Bull. Seismol. Soc. Am.*, *84*, 1608–1649, 1994.

Piper, A. M., et al., Native and contaminated ground waters in the Long Beach–Santa Ana area, California, *U.S. Geol. Surv. Water Supply Pap.*, *1136*, 320 pp., 1953.

Platt, J. P., and C. J. Stuart, Newport-Inglewood fault zone, Los Angeles basin, California: Discussion, *AAPG Bull.*, *58*, 877–883, 1974.

Poland, J. F., Hydrology of the Long Beach–Santa Ana area, California, *U.S. Geol. Surv. Water Supply Pap.*, *1471*, 257 pp., 1959.

Poland, J. F., et al., Ground-water geology of the coastal zone Long Beach–Santa Ana area, California, *U.S. Geol. Surv. Water Supply Pap.*, *1109*, 162 pp., 1956.

Price, E. J., and D. T. Sandwell, Small-scale deformation associated with the 1992 Landers, California, earthquake mapped by synthetic aperture radar interferometry phase gradients, *J. Geophys. Res.*, *103*, 27,001–27,016, 1998.

Rosen, P. A., S. Hensley, I. R. Joughin, F. K. Li, S. N. Madsen, E. Rodriguez, and R. M. Goldstein, Synthetic aperture radar interferometry, *Proc. IEEE*, *88*, 333–382, 2000.

Sandwell, D. T., and E. J. Price, Phase gradient approach to stacking interferograms, *J. Geophys. Res.*, *103*, 30,183–30,204, 1998.

Sandwell, D. T., and L. Sichoix, Topographic phase recovery from stacked ERS interferometry and a low-resolution digital elevation model, *J. Geophys. Res.*, *105*, 28,211–28,222, 2000.

Scharroo, R., and P. N. A. M. Visser, Precise orbit determination and gravity field improvement for the ERS satellites, *J. Geophys. Res.*, *103*, 8113–8127, 1998.

Shaw, J. H., and J. Suppe, Earthquake hazards of active blind-thrust faults under the central Los Angeles basin, California, *J. Geophys. Res.*, *101*, 8623–8642, 1996.

Testa, S. M., E. C. Henry, and D. Hayes, Impact of the Newport-Inglewood structural zone on hydrogeologic mitigation efforts: Los Angeles basin, California, report, pp. 181–203, Assoc. of Ground Water Sci. and Eng., Westerville, Ohio, 1988.

Toppozada, T. R., J. H. Bennett, G. Borchardt, R. Saul, and J. F. Davis, Earthquake planning scenario for a major earthquake on the Newport-Inglewood fault zone, *Calif. Geol.*, *42*, 75–84, 1989.

Walls, C., T. Rockwell, K. Mueller, Y. Bock, S. Williams, J. Pfanner, J. Dolan, and P. Fang, Escape tectonics in the Los Angeles metropolitan region and implications for seismic risk, *Nature*, *394*, 356–360, 1998.

Watson, K. M., SIO InSAR cookbook and investigations of the Newport-Inglewood fault zone, M.Sc. thesis, 107 pp., Univ. of Calif., San Diego, 2001.

Watson, K., Y. Bock, S. Williams, and D. Sandwell, Integrated satellite interferometry: Investigations in the Los Angeles basin, *Eos Trans. AGU*, *79*(45), Fall Meet. Suppl., F184, 1998.

Wilcox, R. E., T. P. Harding, and D. R. Seely, Basic wrench tectonics, *Am. Assoc. Pet. Geol. Bull.*, *57*, 74–96, 1973.

Williams, S., Y. Bock, and P. Fang, Integrated satellite interferometry: Troposphere noise, GPS estimates, and implications for synthetic aperture radar products, *J. Geophys. Res.*, *103*, 27,051–27,067, 1998.

Yeats, R. S., Newport-Inglewood fault zone, Los Angeles basin, California, *Am. Assoc. Pet. Geol. Bull.*, *57*, 117–135, 1973.

Yeats, R. S., Newport-Inglewood fault zone, Los Angeles basin, California: Reply, *AAPG Bull.*, *58*, 884–888, 1974.

Yerkes, R. F., T. H. McCulloh, J. E. Schoellhamer, and J. G. Vedder, Geology of the Los Angeles basin California—An introduction, *U.S. Geol. Surv. Prof. Pap., 420-A*, 57 pp., 1965.

Zebker, H. A., P. A. Rosen, R. M. Goldstein, A. Gabriel, and C. L. Werner, On the derivation of coseismic displacement fields using differential radar interferometry: The Landers earthquake, *J. Geophys. Res.*, *99*, 19,617–19,634, 1994.

Y. Bock, D. T. Sandwell, and K. M. Watson, Cecil H. and Ida M. Green Institute of Geophysics and Planetary Physics, Scripps Institution of Oceanography, University of California, San Diego, 9500 Gilman Drive, La Jolla, CA 92093-0225, USA. (ybock@ucsd.edu; dsandwell@ucsd.edu; kwatson@josh.ucsd.edu)

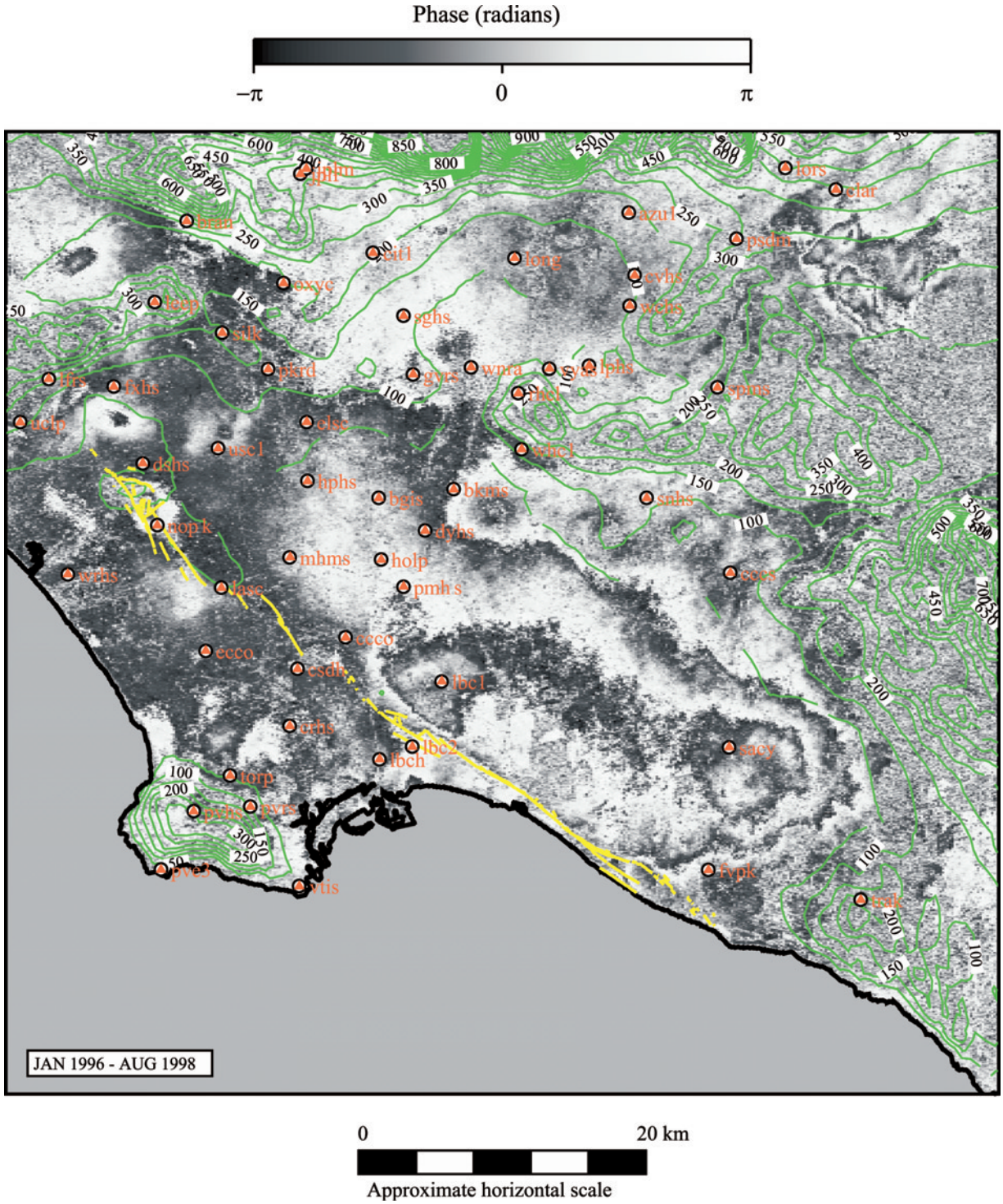

Figure 2. Excerpt of interferogram for ERS-1/2 frame 2925, track 170, orbit pair E1-23705_E2-17559. Also plotted are the coastline (black), SCIGN stations (red), 50-m topographic contours (green), and the NIFZ (yellow).

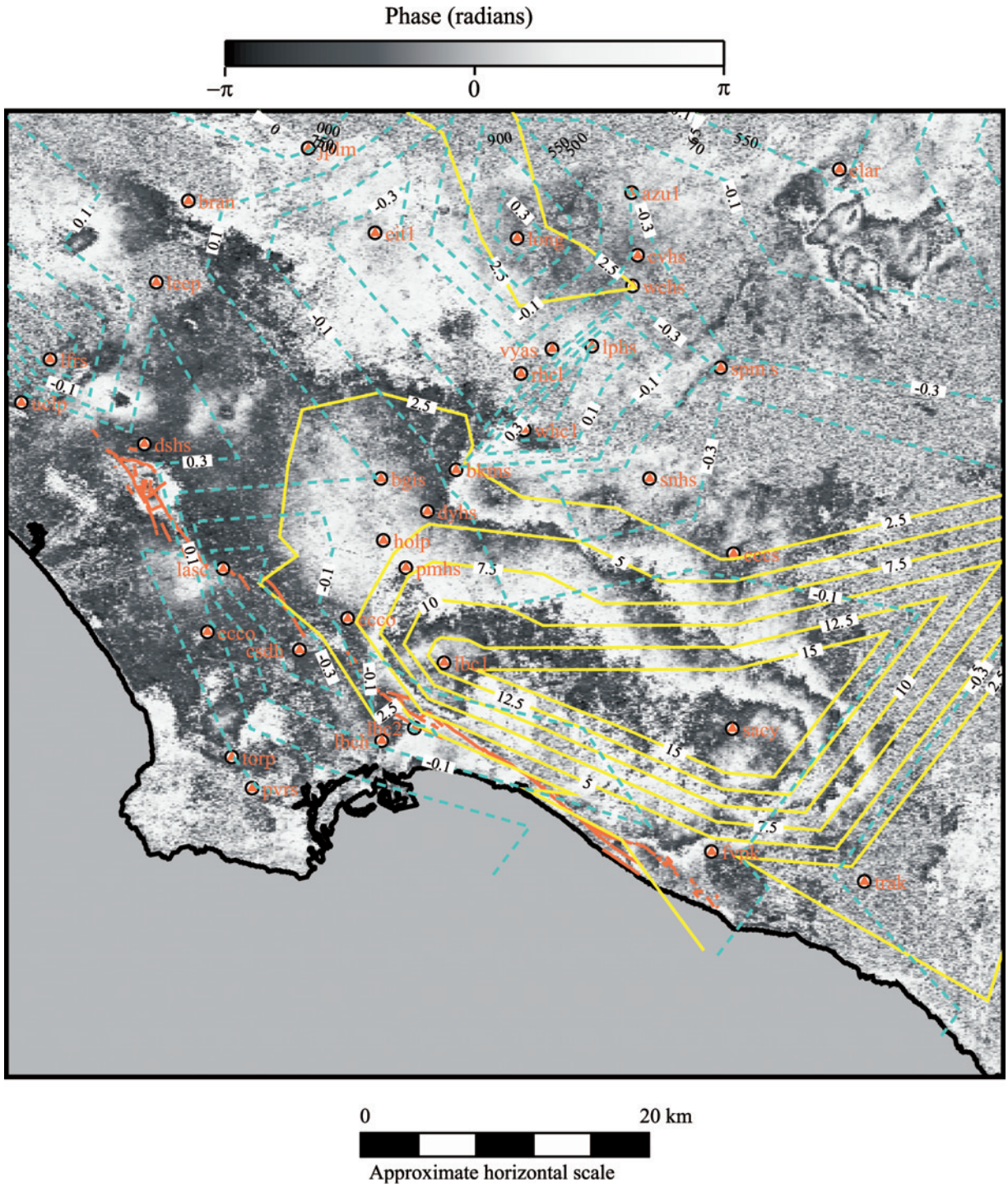

Figure 9. Contour plot of up component least squares fit sinusoidal curve amplitudes (yellow solid lines) in mm and phase (green dashed lines) in years for the SCIGN sites labeled.